

# Metal Injection Molding (MIM) of Mg-Alloys

M. Wolff, J. G. Schaper, M. Dahms, T. Ebel, R. Willumeit-Römer  
and T. Klassen

**Abstract** MIM-technique possesses high potential for the SF<sub>6</sub> free near net shape mass production of small sized and complex shaped parts. Furthermore, MIM involves a high degree of freedom regarding individual alloy- and MMC-composition using the blended elemental (BE-route). Resent research has highlighted MIM of Mg-alloys as highly suitable for biomedical applications like screws, nails and bone-plates, as well as for commercial 3C applications. For prototyping and low quantities, the feedstock can be used for 3D-filament print, too. Hence, demonstrator parts and test specimen could be produced very successfully, ready for industrial upscaling. Increased mechanical properties of MIM dogbone tensile test specimen could be achieved using Mg-2.6Nd-1.3Gd-0.5Zr-0.3Zn alloy (EZK400, UTS: 164 MPa, YS: 123 MPa,  $\epsilon_f$ : 3.4%) and AZ81-alloy for commercial applications (UTS: 240 MPa, YS: 118 MPa,  $\epsilon_f$ : 4%). Thus, the mechanical properties are currently equivalent to those of as cast material and obtaining high development potential.

**Keywords** Metal injection molding · Magnesium · Sintering

---

M. Wolff (✉) · J. G. Schaper · T. Ebel · R. Willumeit-Römer  
Div. Metallic Biomaterials, Helmholtz-Zentrum Geesthacht,  
Centre for Materials and Coastal Research, Institute of Materials Research,  
Max-Planck Str.1, 21502 Geesthacht, Germany  
e-mail: martin.wolff@hzg.de

M. Dahms  
University of Applied Sciences, HS-Flensburg,  
Kanzleistr. 91-93, 24943 Flensburg, Germany

T. Klassen  
Helmut Schmidt University, Holstenhofweg 85, 22043 Hamburg, Germany

## Introduction

Currently, Mg-alloys are becoming more and more attractive for consumer, light-weight [1–3] and biomedical application [4–11]. The new biodegradable and biocompatible Mg-based material shows mechanical properties matching those of cortical bone tissue [12–15]. However, commonly used casting and forging techniques require the use of sulfur hexafluoride ( $\text{SF}_6$ ) as protective gas [16].  $\text{SF}_6$  is a 22800 times more active climate gas than  $\text{CO}_2$  [17]. Hence, the use of  $\text{SF}_6$  in cast-shops will be prohibited within the near future. In contrast, the powder-metallurgical (PM) processing route of metal injection molding (MIM) enable the economic near net shape mass production of complex shaped Mg-alloy parts. The MIM processing requires the manufacturing of a feedstock, consisting of Mg-alloy powder and different polymeric binder components. This feedstock can also be used for the manufacturing of filament, necessary for fused filament fabrication (FFF), commonly known as 3D-printing of filament material. Hence the material can be used for low batches up to high quantities (1piece—1mio. pc. and beyond).

However, sintering of Mg and its alloys was known as not feasible in literature because of a stable oxide layer, sticking on the particle surface and inhibiting the diffusion process, necessary for the sintering [18]. Recent work on sintering of Mg [19–21] and MIM of Mg [22–24] could overcome this major challenge. This study is focusing on the improvement of the full process chain of MIM of new Mg-alloys. In doing so, different test specimen, demonstrator parts and biomedical implant prototypes as shown in Fig. 1 were produced and tested successfully. Sufficient mechanical properties up to 240 MPa UTS, 118 MPa TYS and 4% elongation at fracture could be achieved.

- Right hand side components: feedstock granules made of Mg-alloy powder and binder components.

**Fig. 1** Mg-alloy demonstrator parts and test specimens made by MIM of Mg at Helmholtz-Zentrum Geesthacht



- Upper part: implant screw demonstrator parts in the green and sintered condition (Mg-0.9Ca).
- Middle parts: dogbone tensile test specimen (EZK400) according to ISO 2740-B.
- Lower part: bookmark demonstrator parts (AZ81).

## Materials and Methods

### *Powder, Feedstock and Green Part Production*

For the green part preparation, commercial spherical gas atomized Mg-2.6Nd-1.3Gd-0.5Zr-0.3Zn alloy powder, in the following referred to as EZK400 (product name: MAP+21, Magnesium Elektron, UK) and Mg-8Al-1Zn alloy powder (AZ81, SFM, Martigny, Switzerland) were used for the specimen production. The feedstock was prepared using a binder system consisting of poly-propylene, stearic acid and paraffin wax. The components were blended at approx. 160 °C in a planetary mixer (Thinky ARE-250 planetary mixer, Japan) applying approx. 500G acceleration. To avoid any additional uptake of oxygen, powder handling took place under protective argon atmosphere in a glovebox system (Unilab, MBraun, Germany). Feedstock granules were produced using a cutting mill (Wanner B08.10F, Germany). The green part production of dogbone shape tensile test specimen (ISO 2740-B) and demonstrator parts as shown in Fig. 1 took place using an injection molding machine (Arburg Allrounder 320S) at up to 1500 bar injection pressure, 65 °C mold temperature and 135 °C feedstock temperature. Regarding the state of the art of sintering of magnesium, getter material inside of the labyrinth like crucible configuration has been used [19]. For this purpose, pure irregular coarse magnesium powder grit (Sigma Aldrich, USA) was applied.

### *Debinding and Sintering*

Solvent debinding of stearic acid and organic wax components was done using hexane at 45 °C for 10–15 h (Lömi EBA50/2006, Germany). Thermal debinding of the backbone polymer and consolidation through sintering took place in a combined debinding and sintering hot wall furnace (MUT, Jena, Germany). Thermal debinding was performed in reactive Ar + 5% H<sub>2</sub> gas, using a flow of 1 L/min at 10–60 mbar. Corresponding to former studies about sintering Mg–Ca alloys [19–21], the sintering time was set to 64, 32, 16, 8, 3 and 1 h.

## ***Evaluation of Optimal Sintering Time and Temperature***

For evaluation of optimal sintering time and temperature of the new sinter material, DSC measurements served as a initial analysis (DSC2, Mettler Toledo, Switzerland). Because of the fact that the used MIM-binder-system and the injection molding process steps can influence the sintering performance of the new material, first sintering experiments were performed using the press and sinter (P+S) route to avoid any influences of binder components, debinding solvents and debinding gases. In doing so, the EZK400 powder was pressed to cylindrical compressive strength test specimen (diameter: 8.2 mm; length: 12.5 mm; according to DIN 50106) and micro-tensile test specimen green parts (according to DIN EN 6892-1:2009) using a manual mode press (Enerpac RC 55, USA, applied surface pressure: 100 MPa). To avoid any additional oxygen pick-up, the total powder and specimen handling took place in the glove box system under protective argon atmosphere.

### ***Materials Characterization***

The Archimedes method (Sartorius LA230S, Germany) was applied to measure the residual porosity of the sintered parts. Geometrical data calculation (Mahr 16EX, calliper, Germany) were performed to measure shrinkage and density, too. The microstructure was investigated, using SEM (Zeiss DSM 962, Germany) and EDS mapping. Compressive and tensile tests of sintered P+S as well as MIM specimens were performed using a Schenck Trebel RM100 materials testing machine.

## **Results and Discussion**

### ***Sintering Temperature and Time***

The DSC-analysis of the commercial Mg-alloy powder EZK400 presented a liquidus temperature of approx. 635 °C (mean value of: 631–640 °C) as shown in the diagram in Fig. 2.

This first DSC result was used for the approximated setting of the initial sintering temperature. As a result, a sintering temperature of 635 °C was chosen as a good compromise in view of the following two aspects: The higher the sintering temperature, the exponentially higher is the diffusion activity between the particles. Hence, sintering time can be reduced drastically using marginal higher sintering temperature. On the other hand, the higher the sintering temperature, the higher is the amount of transient or permanent liquid phase in the compound. Hence, the part can lose its shape or liquid phase can pour out of the part. As mentioned above, first

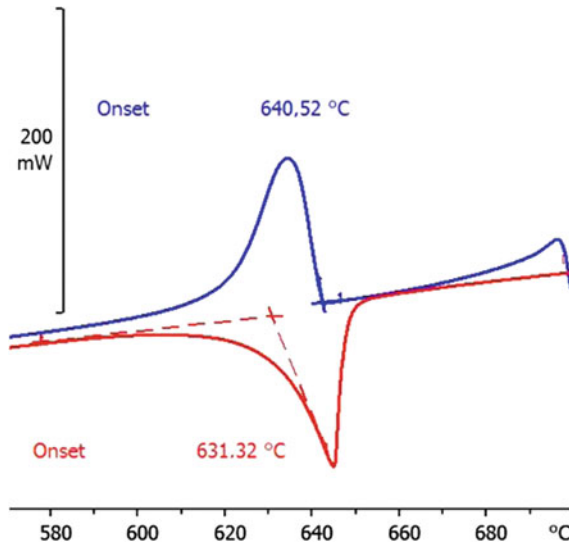


**Fig. 2** DSC-analysis of EZK400 alloy powder using a heating rate of 5 K/min

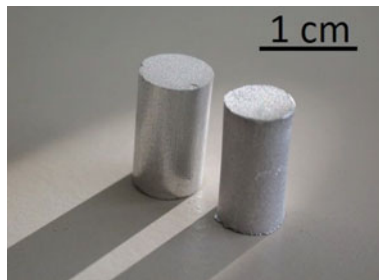


**Fig. 3** Cylindrical compressive test specimen made of EZK400 in the green condition (left) and the as sintered condition (right) showing significant shrinkage

sintering experiments on cylindrical compressive test specimen as shown in Fig. 3 and micro-tensile test specimen were performed using binder free P+S technique.

The following diagram in Fig. 4 shows the micro-tensile test results of the first three sets of the P+S specimen sintered at 635 °C at different sintering times. The new EZK400 material is sintering with permanent liquid phase. Hence, the sintering time could be reduced significantly in comparison to former experiments using 64 h of sintering time.

The first set of columns in the diagram displays that 1 h of sintering time is insufficient for the nearly dense consolidation of the part. Only  $1.1 \pm 0.2\%$  of elongation at fracture and  $124 \pm 6$  MPa UTS were achieved. In contrast, using 16 h of sintering time,  $188 \pm 5$  MPa UTS and 5.8% elongation at fracture could be

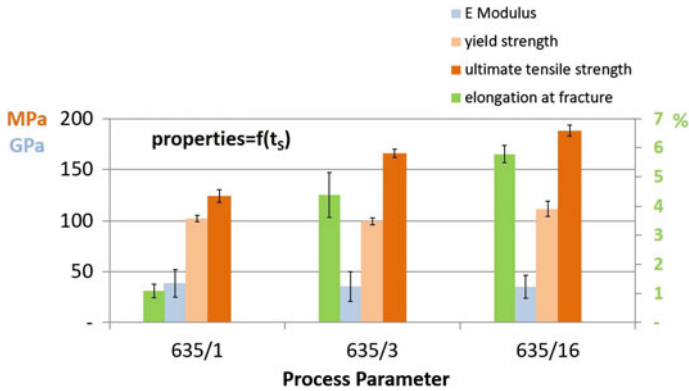


**Fig. 4** Mechanical properties of micro-tensile test specimen produces by P+S, using a fixed sintering temperature of 635 °C and varying sintering time

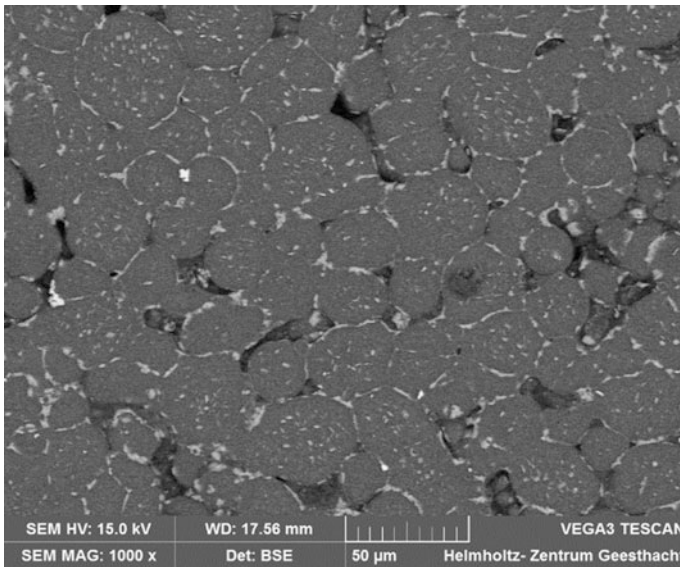


**Fig. 5** SEM micrograph of the EZK400 alloy, sintered for 1 h

reached. Moreover, significant improvement of mechanical properties could be achieved even by use of an economic short sintering time of 3 h. The third set of columns displays sufficient material properties showing  $4.4 \pm 0.8\%$  of elongation at fracture, and above  $166 \pm 4$  MPa UTS. The following images in Figs. 5 and 6 shall give an overview about the microstructure of the material in the as sintered condition for the shortest chosen sintering time of 1 h as shown in Fig. 5 and the longest chosen sintering time of 64 h as shown in Fig. 6. The microstructure of the

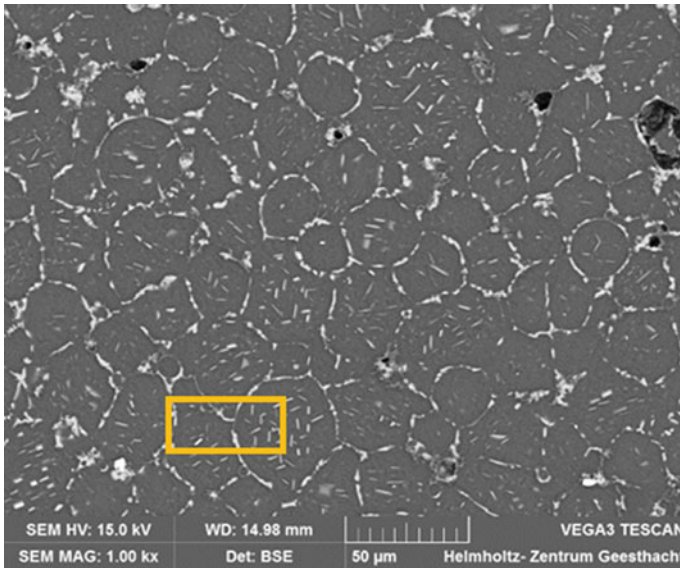


**Fig. 6** SEM micrograph of the EZK400 alloy, sintered for 64 h

EZK400 material, sintered for 1 h, as shown in Fig. 5 is in accordance to the mechanical properties, shown in the first set of columns of Fig. 4. It can be seen that the material is not fully consolidated, presenting a residual porosity of around 7%.

In contrast, the following Fig. 6 reveals the microstructure of the material, sintered for 64 h, which presents only  $0.7 \pm 0.1\%$  of residual porosity.

Because of the fact that sintering time can influence the densification of the compound maximum in a linear behavior, a second set of sintering operations was done for further optimization of the sintering regime. In doing so, a fixed sintering time of 3 h and variation of the sintering temperature between 635 and 643 °C as shown in Fig. 7 were chosen. As a result, the mechanical properties of the material could be improved significantly using the economic sintering time of 3 h at 643 °C as shown in the third set of columns in Fig. 7. Hence, maximum UTS of  $188 \pm 4$  MPa at  $5 \pm 1\%$  of elongation at fracture and  $122 \pm 6$  MPa yield strength were achieved.

Moreover, the sintering performance of the new EZK400 material was as good, that sintering could be performed without getter material inside of the crucible setup resulting in no significant loss of mechanical strength, as shown in the fourth set of columns in Fig. 7. This is in contrast to the state of the art for sintering of magnesium, where getter material inside the labyrinth-like crucible configuration has to be used [19]. The fast sintering performance of the EZK400 material might be explained on the ground of attendance of permanent rare earth rich liquid phase during sintering. The orange rectangle in Figs. 6 and 8A displays the area of an EDX-mapping analysis, performed on the EZK400 material, sintered for 64 h.

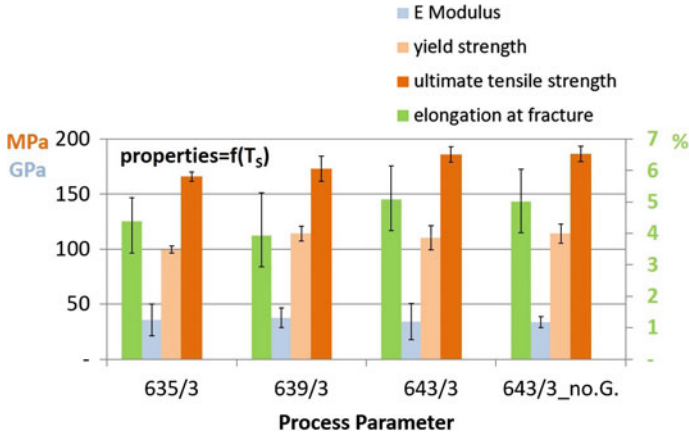


**Fig. 7** Mechanical properties of micro-tensile test specimen produces by P+S, using a fixed sintering time of 3 h and variation sintering temperature

As shown in the SEM images and EDX mapping analyses in Fig. 8a–f, the former particle boundaries (yellow arrows) mainly consists of Gd-, Nd- and Zr-rich phases, combined with an increased level of oxygen (O). The needle shape bright crystal structure inside of the roundish particle structure (red arrows in Fig. 8a) can be allocated to  $Mg_5Gd$  and  $MgNd_5$  intermetallic, as well as to mixed Mg-RE-oxides. In contrast, the bright secondary phases on the particle boundaries/grain boundaries display additional zirconium (Zr) (Fig. 8a, e) and increased

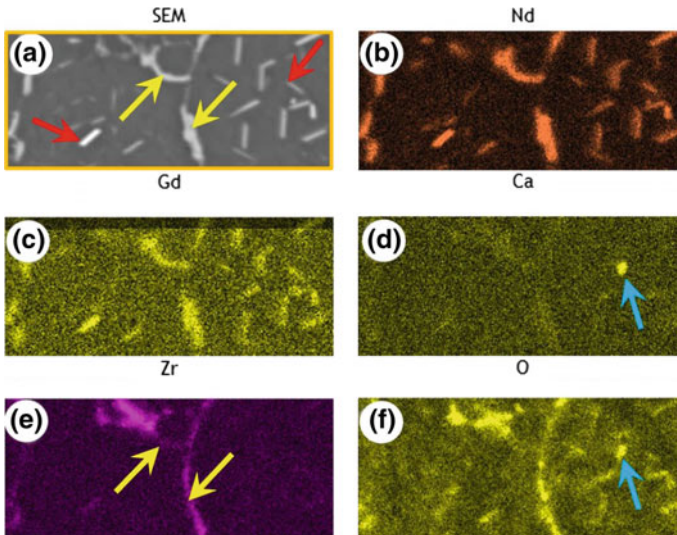


**Fig. 8** SEM image and EDX mapping of the EZK400 material, sintered for 64 h



intensity of oxygen. The single bright oxygen dot inside of the roundish particle in Fig. 8d, f and a (blue arrow) can be identified as a CaO rich artefact onto the specimen's surface. However, for clear identification of these different phases in the as sintered EZK400 microstructure, nano-diffraction analysis, using synchrotron radiation might be a sufficient tool for further investigations.

How does the fast sintering of the EZK400 material occur? It can be assumed on the one hand that, if the powder particle surface is coated by magnesium oxide in the as received condition, the rare earth rich permanent liquid phases might be able to reduce this MgO-layer material in accordance to the relationship of Gibbs free energy of oxide formation. On the other hand, if rare earth rich oxides coat the particle surfaces of the used powder, Mg might be able to reduce these oxides, too. To answer this question in more detail, an adequate surface analysis of the particle surface, e.g. XPS, IR-spectroscopy or  $\mu$ -XRF, in combination with DSC and XRD-analyses have to be done in future work. Regarding the sintering performance of Mg–Ca alloys, literature reveals that during magnesium oxide layer reduction as shown in the following Eq. 1:



The shown redox reaction takes place, in dependency of element concentration, in both directions [25].

### ***Sintering of MIM EZK400 Parts***

In a further step, the sintering results of the prior chapter were adapted to the sintering of parts, produced by metal injection molding (MIM) as shown exemplary in Fig. 1 and the following Fig. 9. As shown in these images, the demonstrator parts and dogbone shape tensile test specimens exhibit significant shrinkage and a perfect smooth, silver shade surface. The tensile test results of the dogbone shape specimen, as shown in Fig. 1, reveal UTS of 161 MPa, yield strength of 123 MPa and elongation at fracture of 3.4%. The following diagram in Fig. 10 compares the

**Fig. 9** Suture anchor implant screw demonstrator part made by MIM of EZK400 material. Design: ConMed, USA



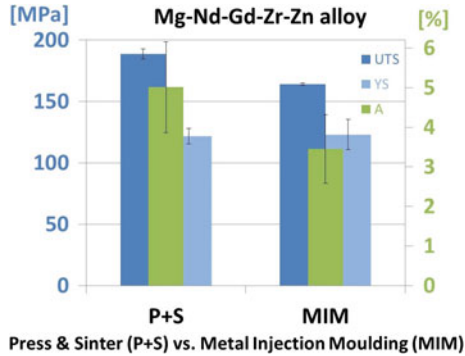


**Fig. 10** Comparison of tensile test results of the EZK400 material using the P+S route in comparison to MIM

mechanical test results of EZK400 material of the P+S route to the MIM processed material.

The diagram points out that MIM processed material could achieve 87% of the UTS of the P+S processed material and 69% of the elongation at fracture of the P+S processed material. However, the yield strength of the MIM processed material is the same of the P+S processed material. The decrease in strength and ductility using the MIM-route in comparison to the P+S route can be explained by formation of additional needle shape crystals, forming a ring shape structure in the near grain boundary region of each grain/ancient powder particle in the microstructure, as shown in the following Fig. 11.

A feasible explanation of this phenomenon might be the formation of carbide phases during thermal debinding of the green part by chemical reaction of reactive, carbon rich debinding gases with rare earth alloying elements. Hence, this needle shape phase might consist of  $ZrC$ , or even Nd- and Gd-containing composite carbides. To avoid this weakening phenomenon of the material, different techniques can be used:

- The thermal debinding step has to be optimized. If it is possible to fulfill the binder decomposition in a certain temperature range in which carbide formation does not take place, the formation of this phase can be avoided.
- Thermal debinding in hydrogen atmosphere.
- Performing T4 solid solution and T6 ageing heat treatment to induce a homogeneous distribution of the new carbide phase in the microstructure.

If the second technique will be of success, even better mechanical properties in comparison to the P+S material could be achieved through precipitation hardening effects.

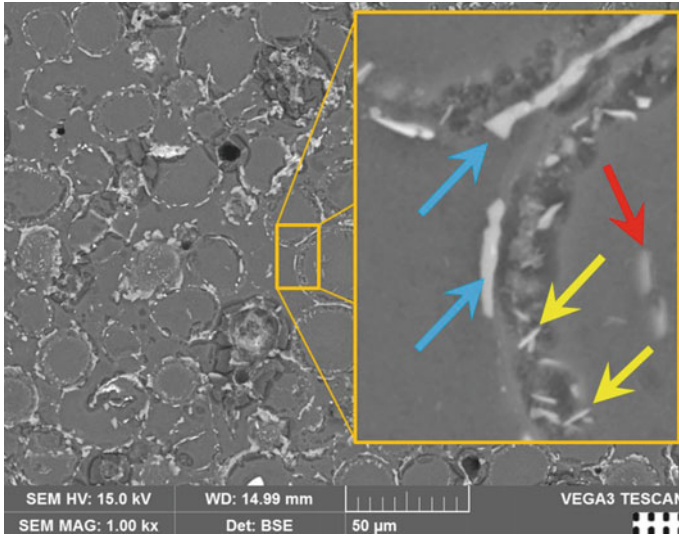


**Fig. 11** Microstructure of MIM processed EZK400 showing secondary phases onto grain boundaries (blue arrows) and needle shape phases inside of the roundish grains (red arrow), as well as new near grain boundary needle shape phases (yellow arrows)

### *Sintering of MIM AZ81 Parts*

Next to the EZK400 alloy powder, the commercial Mg-alloy powder AZ81 was tested, too. Dogbone shape tensile test specimens revealed UTS of  $240 \pm 6$  MPa, yield strength of  $118 \pm 2$  MPa and elongation at fracture of  $5.1 \pm 0.6\%$ . The following Fig. 12 displays an SEM image of the microstructure of the as-sintered AZ81 material.

In comparison to the EZK400 material, the AZ81 material contained significantly less secondary phases being homogeneously distributed along the grain boundaries. Original powder particles, connected through liquid phase sintering, are still visible. The AZ81 could be sintered very successful achieving a residual porosity of 4.4% (see black dots).

### **Conclusions and Outlook**

This study points out that Mg alloys like Mg-2.6Nd-1.3Gd-0.5Z-0.3Zn (EZK400) and AZ81 can be sufficiently sintered under SF<sub>6</sub>-free and economic conditions. Before, this was known only for stainless steel, titanium alloys or hard metals. The optimal sintering regime for the novel EZK400 Mg-alloy powder could be found to be 643 °C for 3 h. Applying this parameter set and using pressed and sintered

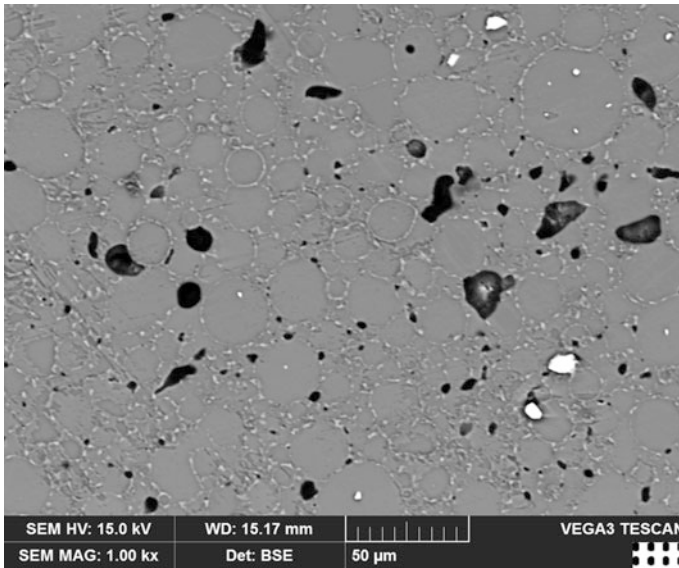


**Fig. 12** Microstructure of MIM processed AZ81 showing 4.4% residual porosity and secondary phases on grain boundaries

(P+S) tensile test specimens, sound UTS of 188 MPa and 5% elongation at fracture could be achieved. Using MIM parts an UTS of 164 MPa and 3.4% elongation at fracture were determined. The discrepancy in UTS and elongation at fracture can be explained due to formation of additional secondary phases in the near grain boundary region. These phases are assumed to be carbides, formed during thermal debinding of the brown part. Further work shall identify these phases using adequate surface analysis technique of the particle surface, e.g. XPS, IR-spectroscopy and  $\mu$ -XRF, in combination with DSC and XRD-analysis, as well as synchrotron based high-energy X-ray nano-diffraction. Moreover, this study discusses techniques to avoid these additional phases.

Furthermore, other Mg-alloy powders such as commercial AZ81 could be successfully processed by MIM, too, and an UTS of 240 MPa could be achieved. Generally, MIM processing of Mg-alloy powders implements economic and SF<sub>6</sub>-free near net shape mass production of small sized complex Mg-alloy parts.

## References

1. Friedrich HE, Mordike BL (2006) Springer, Berlin, Germany
2. Kainer KU (2010) Wiley-VCH, Weinheim, Germany
3. Dieringa H, Hort N, Kainer KU (2011) Proceedings of LMT 2011, vol. 690. Trans Tech Publications Ltd, Material Science Forum

4. Li Z, Gu X, Lou S, Zheng Y (2008) The development of binary Mg-Ca alloys for use as biodegradable materials within bone. *Biomaterials* 29:1329–1344
5. Staiger MP, Pietak AM, Huadmai J, Dias G (2006) Magnesium and its alloys as orthopaedic biomaterials- a review. *Biomaterials* 27:1728–1734
6. Witte F, Kaese V, Haferkamp H, Switzer E, Meyer-Lindenberg A, Wirth CJ, Windhagen H (2005) *Biomaterials* 26:3557–3563
7. Witte F, Reifenrath J, Müller PP, Crostack H-A, Nellesen J, Bach FW, Bormann D, Rudert M (2006) *Materialwissenschaft und Werkstofftechnik* 37:504–508
8. Witte F, Feyerabend F, Maier P, Fischer J, Störmer M, Blawert C, Dietzel W, Hort N (2007) *Biomaterials* 28:2163–2174
9. Witte F, Ulrich H, Rudert M, Willbold E (2007) *J Biomed Mater Res* 81A:748–756
10. Witte F, Fischer J, Nellesen J, Crostack HA, Kraese V, Pisch A, Beckmann F, Windhagen H (2006) *Biomaterials* 27:1013–1018
11. Witte F, Ulrich H, Palm C, Willbold E (2007) *J Biomed Mater Res* 81A:757–765
12. Poumarat G, Squire P (1993) *Biomaterials* 14:337–349
13. Cunha AR et al (2012) *Int J Hypertens*. Hindawi Publishing Co. Art. ID: 754250
14. Janning C, Willbold E, Vogt C, Nellesen J, Meyer-Lindenberg A, Windbergen H, Thorey F, Witte F (2010) Magnesium hydroxide temporarily enhancing osteoblast activity and decreasing the osteoclast number in peri-implant bone remodelling. *Acta Biomaterialica* 6:68–1861
15. Witte F, Fischer J, Nellesen J, Crostack HA, Kraese V, Pisch A, Beckmann F, Windhagen H (2006) In vitro and in vivo corrosion measurements of magnesium alloys. *Biomaterials* 27:1013–1018
16. *Magnesium Taschenbuch* (2000) Aluminium Verlag Düsseldorf, 1st edn, p 466ff. ISBN: 3-87017-264-9
17. Statistisches Bundesamt (2014) Erhebung bestimmter klimawirksamer Stoffe “Schwefelhexafluorid” (SF<sub>6</sub>), Wiesbaden. [www.destatis.de](http://www.destatis.de), Artikelnummer: 5332401-13700-4
18. Hort N, Dieringa H, Kumar ST, Kainer KU (2006) *Magnesium matrix composites*. Springer, Berlin, p 237
19. Wolff M, Dahms M, Ebel T (2010) Sintering of magnesium. *Adv Eng Mater* 12:829–836
20. Wolff M, Guelck T, Ebel T (2009) Sintering of Mg and Mg-Ca alloys for biomedical applications. *Euro PM2009 Proceed* 2:417–422
21. Wolff M, Bischof C, Dahms M, Ebel T, Klassen T (2012) 9th International conference on magnesium and their applications. Vancouver, Canada 8–12 July 2012, p 102
22. Wolff M, Schaper JG, Dahms M, Ebel T, Kainer KU, Klassen T (2014) *Powder Metall* 57 (5):331–340
23. Wolff M, Schaper JG, Suckert MR, Dahms M, Feyerabend F, Ebel T, Willumeit-Römer R, Klassen T (2016) Metal injection molding (MIM) of magnesium and its alloys. *Metals* 6(118). <https://doi.org/10.3390/met6050118>
24. Wolff M, Schaper JG, Suckert MR, Dahms M, Ebel T, Willumeit-Römer R, Klassen T (2016) Magnesium powder injection molding (MIM) of orthopedic implants for biomedical application. *JOM* 68(4). <https://doi.org/10.1007/s11837-016-1837-x>
25. Wiese B (2017) The effect of CaO on magnesium and magnesium calcium alloys. Universitätsbibliothek der TU Clausthal. <https://doi.org/10.21268/20170504133828>